Carbohydrate Polymers 352 (2025) 123180

Contents lists available at ScienceDirect

Carbohydrate Polymers

journal homepage: www.elsevier.com/locate/carbpol

Dynamic mechanical analysis of alginate/gellan hydrogels under controlled conditions relevant to environmentally sensitive applications

Juan Pablo Segovia-Gutiérrez [a], José Alberto Rodríguez Agudo [b], Nicolas Binder [b], Peter Georg Weidler [c], Frank Kirschhöfer [c], Claudia Fink-Straube [d], Jürgen Utz [b], Natalie Germann [a,*]

[a] Institute of Process Systems Engineering, University of Stuttgart, Böblinger Str. 78, 70199 Stuttgart, Germany
[b] Anton Paar Germany GmbH, Hellmuth-Hirth-Strasse 6, 73760, Ostfildern-Scharnhausen, Germany
[c] Institute of Functional Interfaces, Karlsruhe Institute of Technology, Hermann-von-Helmholtz-Platz 1, 76344 Eggenstein-Leopoldshafen, Germany
[d] Leibniz Institute of New Materials, Campus D2 2, 66123 Saarbrücken, Germany

ARTICLE INFO

Keywords:
Hydrogel
Temperature
Relative humidity
Mechanical properties
Rheometry
Mesoporous silica particles
Alginate
Gellan
Water-based materials

ABSTRACT

Hydrogels are natural/synthetic polymer-based materials with a large percentage of water content, usually above 80 %, and are suitable for many application fields such as wearable sensors, biomedicine, cosmetics, agriculture, etc. However, their performance is susceptible to environmental changes in temperature, relative humidity, and mechanical deformation due to their aqueous and soft nature. We investigate the mechanical response of both filled and unfilled alginate/gellan hydrogels using a combined axial-torsional rheometric approach with cylindrical samples of large length/diameter ratio under controlled temperature and relative humidity. Dynamic Mechanical Analysis (DMA) is performed on the same specimen in both torsion and extension under identical experimental conditions. This rheometric approach ensures consistent initial and boundary conditions, which are essential for a reliable estimation of viscoelastic moduli G^* and E^*, and their dependence on temperature, frequency, and relative humidity. Our findings indicate that humidity critically affects the mechanical response of the material due to sample volume shrinkage, necessitating corrections to the viscoelastic moduli. We also find temperature plays a role only at low/medium relative humidity values. The inclusion of fillers leads to a modest increase in the elasticity of the hydrogel, probably due to restricted water diffusion out of the sample. In connection with the latest, unfilled samples in breaking tests present only slippage due to twist-induced surface water excess, opposite to breakage events shown by filled samples, probably linked to restricted water diffusion.

1. Introduction

Hydrogels are water-based polymeric networks that can swell or shrink in a high-volume fraction without losing their physical integrity (Ahmed, 2015). From an applicability perspective, hydrogels are very suitable materials due to the versatility of the synthesis routes involved and the wide variety of natural and synthetic polymers available. Therefore, hydrogels are considered as key components in many different practical areas such as wearable sensors (Dong et al., 2023; Wu et al., 2024), electronic devices (Anjum et al., 2021; Dutta et al., 2024), biomedicine (Jridi et al., 2015; Subramani et al., 2020: Wang et al., 2023), optics (Chervinskii et al., 2021), agriculture (Vedovello et al., 2024), among others.

Certain types of conductive hydrogels are currently used as wearable sensors due to their flexibility and good adhesion. However, as they are often exposed to environmental changes in temperature and relative humidity, these hydrogel-based wearable sensors can have some drawbacks, such as dehydration, loss of mechanical performance, etc. Therefore, these drawbacks can limit long-term wear or reduce the durability of the sensors. For example, wearable sensors based on xanthan collagen nanosilver hydrogels exhibit a reduction in tensile strength when exposed to varying temperatures, together with fluctuating water retention capabilities (Dong et al., 2023). Interestingly, the mechanical performance was improved by the addition of plant fibres

* Corresponding author.
E-mail addresses: juanpablo.segovia@svt.uni-stuttgart.de (J.P. Segovia-Gutiérrez), jose.rodriguez@anton-paar.com (J.A.R. Agudo), nicolas.binder@anton-paar.com (N. Binder), peter.weidler@kit.edu (P.G. Weidler), frank.kirschhoefer@kit.edu (F. Kirschhöfer), claudia.fink-straube@leibniz-inm.de (C. Fink-Straube), juergen.utz@anton-paar.com (J. Utz), natalie.germann@svt.uni-stuttgart.de (N. Germann).

https://doi.org/10.1016/j.carbpol.2024.123180
Received 5 November 2024; Received in revised form 18 December 2024; Accepted 20 December 2024
Available online 30 December 2024

and polysaccharides. Wearable sensors are usually in direct contact with the skin and need to be designed to ensure breathability, but also moisture resistance to maintain the device's shelf life. This is particularly relevant for hydrogel-based oxygen sensors in high humidity environments (Wu et al., 2024). On the other hand, the design of wearable sensors should aim for an acceptable match between the mechanical properties of the sensor and the skin to reduce the influence of the skin on the sensor.

In conventional electronics, the materials used are rigid and brittle, limiting their design to certain types of applications. In recent years, the incorporation of flexible, softer and lighter materials with electrochemical properties into electronics manufacturing has significantly broadened the range of applications. This is the case of polyvinyl alcohol and phosphoric acid (PVA- H_3PO_4) hydrogel polymer electrolytes as flexible supercapacitors (Anjum et al., 2021). The mechanical properties, conductivity and capacitance of these flexible supercapacitors are strongly dependent on the relative humidity. The Young's modulus, for instance, shows a significant decrease when the relative humidity changes between 30 % and 60 %. Conversely, both conductivity and capacitance increase. The loss of mechanical stability due to high water content can be overcome, or at least improved, by varying the cross-linking density and selecting the appropriate type of monomer, or by adding dopants (Dutta et al., 2024).

Hydrogels prepared from biopolymers have been used extensively in biomedicine as topical dressings due to their biocompatibility, biodegradability and suitability for the delivery of drugs (Brumberg et al., 2021; Mayer et al., 2021; Wang et al., 2023). As in the case of wearable sensors, topical dressings are in direct contact with human skin, which has a temperature of approximately 30 °C. At the same time, they are exposed to air with broad relative humidity and temperature variations. When the hydrogel is exposed to such conditions, it can suffer from swelling or evaporation (Jridi et al., 2015), affecting its mechanical properties. A decrease in elasticity with an increase in phosphate buffered saline retention after immersion has been observed in polyacrylamide hydrogels (Subramani et al., 2020), with variation also dependent on hydrogel composition.

In the field of optics, temperature and relative humidity also play a key role. For example, poly(N-isopropylacrylamide)–acrylamidobenzophenone (PNIPAm)-based hydrogels have been used in metal-hydrogel-metal reflective filters to reversibly tune the optical resonance through their swelling/deswelling ability (Chervinskii et al., 2021). By keeping the relative humidity constant at 80 % and deswelling the hydrogel by raising the temperature to 45 °C, the authors showed that this resulted in a blue shift in the optical resonance. The reverse effect, i.e. a red shift of the optical resonance, was also demonstrated by lowering the temperature. Mechanical stability must be considered in the design of such hydrogels to withstand multiple swelling/deswelling cycles.

In agriculture, global desertification has become a major concern for food production. Interestingly, hydrogels offer great advantages by increasing soil germination, facilitating plant growth and conserving water through swelling (Vedovello et al., 2024). This would allow water to be stored and released in a controlled manner during periods of drought, thereby increasing the efficiency of water resource use. Again, the mechanical stability of the hydrogels is critical to prolonging their shelf life.

Mechanical integrity of hydrogels can be compromised when subjected to varying temperature and relative humidity conditions, therefore shortening the shelf-life of the material, or impoverishing the performance of the application. The addition of different types of fillers is often considered to introduce new functionalities or to improve mechanical stability. Their size, concentration, and surface chemistry have a major impact on the overall mechanical performance of hydrogels. For example, in acrylamide-based hydrogels, Young's modulus and toughness increase when the diameter of the silica particles is reduced from 50 μm to 75 nm (Hu & Qu, 2019). In a native gelatin-based hydrogel filled with glass beads with diameters between 8 and 12 μm, a significant reduction in the viscoelastic modulus was observed at the highest bead fraction of 1 %. This could be due to the observed formation of local particle clusters, which introduce a discontinuity in the gelatin network and thus weaken it (Goudoulas & Germann, 2019). Nanoporous silica microparticles have been combined with a hydrogel of oxidized hyaluronic acid and adipic acid dihydrazide. Negatively charged Si-O-Si and Si-OH groups were generated on the surface of the microparticles by chemical oxidation with H_2O_2. The electrostatic interactions between negatively charged groups and positively charged nitrogen bonds of the hydrogel led to an enhancement of the interaction between the microparticles and the polymer network of the hydrogel, resulting in an improvement of the mechanical properties (França et al., 2021). Fillers porosity at the mesoporous level is another significant property, which would allow the particles to be loaded with therapeutic agents that can be released under certain conditions (Mori et al., 2014).

Hydrogels used in the above applications have a large percentage of their surface area exposed to specific temperatures and relative humidities, facilitating water and heat exchange with the environment. This suggests that mechanical characterization should be carried out by exposing a larger percentage of the surface area of the hydrogel to the environment to simulate the conditions of use. However, most publications investigating the mechanical properties of hydrogels consider plate-plate geometries with small gaps where the fraction of exposed surface is minimal. An alternative would be to use solid circular fixtures for cylindrical samples with a large L/D ratio, where L is their length and D is their diameter, to increase the exposed surface area. Furthermore, with this sample geometry, the measured extensional modulus remains independent of the L/D ratio. Compared to classical squeeze flow experiments on hydrogels with parallel plates, this is a thus significant advantage (Wingstrand et al., 2016). Ed-Daoui and Snabre (2021) tested cylindrical samples of agarose hydrogels under different compressive loading speeds and simultaneously recorded the changes in hydrogel volume to determine Poisson's ratio. Amiri et al. (2023) used a semi-analytical method and ran COMSOL-Multiphysics simulations to study the coupled extension-torsion deformation of cylindrical hydrogels. They showed that the transient behavior of the cylindrical sample is highly dependent on the deformation rate and material properties. Mollica et al. (2012) applied the continuum mixing theory to study the stress relaxation of cylindrical hydrogels subjected to combined torsion and extension, where the different relaxations are directly or indirectly related to the solvent outflow due to sample twisting. Although these studies show the strong influence of temperature and humidity on hydrogel mechanics, the literature lacks systematic dynamic data with absolute values for tensile and shear moduli measured on the same samples under controlled environments.

In the current work, we present a systematic advanced rheometric study of alginate/gellan gels unfilled/filled with mesoporous silica particles subjected to different types of mechanical deformations (extension/torsion) in the linear and nonlinear viscoelastic range under different temperatures and relative humidity. A combined axial-torsional rheometer is used for this purpose. This type of device has recently proven useful for measuring the dynamic extensional modulus, E^*, and the torsional shear modulus, G^*, from a single specimen in a single measurement and under the same experimental conditions for the case of isotropic specimens (Kim et al., 2024; Rodríguez-Agudo et al., 2023). This type of measurement of two independent moduli, according to the so-called standard or Tschoegl protocol, guarantees identical initial and boundary conditions (Tschoegl et al., 2002). It is therefore essential for the indirect measurement of G^* and E^* as a function of frequency and temperature with sufficient accuracy and precision. In this paper, we extend this type of measurement to hydrogels by adding other environmental factors such as humidity to the protocol. The choice of alginate/gellan as hydrogel was based on several important features (Hazur et al., 2020). For instance, this biocompatible hydrogel model system is well-shear-thinning and has therefore been proposed for bio-

printing. Besides biocompatibility, the selection of the crosslinker is also crucial for bio-printing. Here, $CaCO_3$ induces a moderately fast gelation with the aid of Glucono-δ-lactone, resulting in a more homogeneous microstructure. This is in contrast, for instance, to the fast gelation of sodium alginate observed when $CaCl_2$ is used as a crosslinker (Besiri et al., 2020). Gellan is often used for tissue engineering, and the interpenetrating network nature of the proposed hydrogel allows easy tuning of material properties by adjusting the relative composition of components. On the other hand, the selection of mesoporous silica particles as fillers was also based on several relevant characteristics (Mori et al., 2014), such as non-toxicity, biocompatibility, and biodegradability. From a morphological point of view, mesoporous silica particles also present a large surface area, high pore volume, controllable pore sizes, and surface chemistry.

Our hypothesis is that the rheometric approach presented here, based on dynamic mechanical analysis, which is conventionally used for solid materials such as elastomers, plastic parts, metals, etc., can be extended to softer materials such as hydrogels, and that a complete mechanical characterization can be obtained. We also hypothesize that this approach has advantages over parallel plate squeeze-flow tests, such as providing a larger sample surface exposed to the environment to facilitate water and heat exchange; determining torsional and extensional moduli with sufficient accuracy and precision, under the same exact environmental conditions, in a continuous measurement run. Importantly, our hypothesis is supported by structural analysis of the different hydrogels using infrared spectroscopy and X-ray diffraction to link both the microscopic level and the macroscopic rheometric response. Finally, the current work can also be considered an important and natural step forward with respect to recent field-relevant publications (Kim et al., 2024; Rodríguez-Agudo et al., 2023).

2. Materials and methods

2.1. Materials

Gellan (Cat. No. J63423.30), with a molecular weight of $(1.83 \pm 0.07) \times 10^6$ Da, and calcium carbonate ($CaCO_3$) (Cat. No. 33295) were purchased from Thermo Scientific. Glucono-δ-lactone (GDL) (Cat. No. G2164-100G), powdered 1 μm mesoporous silica particles (Cat. No. SIAL806889-1G) were purchased from Sigma Aldrich. Sodium alginate (Alg) (Cat. No. A3249,0250) with a molecular weight of $(6.105 \pm 0.007) \times 10^5$ Da, high guluronic acid (G) residue content and corresponding M/G ratio of 1.38 was obtained from PanReac AppliChem (Zvicer et al., 2019).

2.1.1. Preparation of unfilled hydrogels

Two unfilled hydrogels were prepared, one composed of a mixture of Alg and gellan and another one with gellan only. The corresponding proportions of the different components involved in the hydrogel synthesis were chosen to prepare 100 ml batches, similar to those in (Li et al., 2020). A volume of 90 ml of double-distilled water was poured into a borosilicate glass beaker (VWR) with a capacity of 150 ml, then placed in a thermal bath and heated to 80 °C using a magnetic stirring heating plate (VWR Advanced VMS-C7). Once the temperature of the water reached 80 °C, a total concentration of 2 % (*w/v*) polysaccharides was added. In the case of the hydrogel composed of the mixture of Alg and gellan, the ratio was 2:8. For the pure gellan gel; the ratio was 0:10. The baker was sealed with a plastic sealing film (Seal-R-film™) to avoid water loss.

The mixture was kept at 80 °C for 3 h under moderate continuous stirring, with a rotational speed of 2.5 on the magnetic stirring heating plate scale, to ensure complete dissolution and hydration of the polysaccharides. After 3 h of stirring at 80 °C, no visible polysaccharide lumps were visible, and the temperature was set to 50 °C. The solutions with the crosslinking agents were prepared as follows: 0.5 g of GDL was dissolved in 5 ml of double-distilled water, and 0.3 g of $CaCO_3$ was dispersed in 5 ml of double-distilled water. While keeping the temperature at 50 °C, 5 ml of the GDL solution was added to the polysaccharide solution, and the mixture was vigorously stirred to ensure homogeneity. Afterward, 5 ml of the $CaCO_3$ dispersion was added, and again, the mixture was vigorously stirred. After an additional 30 min, the temperature of the sample was cooled to room temperature to reach the final gel state. Unfilled hydrogels were stored in a lab refrigerator until measurements were performed.

2.1.2. Preparation of hydrogel filled with particles

The preparation of the hydrogel with particles with a final particle content of 0.7 % (w/v) was the same as in the case of the pure hydrogel, except for the intermediate step of adding the particles. The particles were prepared by dispersing 0.7 g of the powder in 2 ml of double-distilled water. Subtle shaking was performed in an ultrasonic bath for 30 to 60 s to break up the visible aggregates. The particle dispersion was then added to the polysaccharide solution after being stirred at 80 °C for 3 h, and the mixture was stirred by hand until a clear homogeneous dispersion was obtained. The particles were added at this stage of the process because the polysaccharide solution had a lower viscosity at this temperature, which facilitated redispersion. The subsequent preparation steps were the same as those described for the pure hydrogel. Finally, filled hydrogels were stored in a lab refrigerator until measurements were performed.

2.1.3. Sample preparation for Gel Permeation Chromatography (GPC)

20 mg of each sample was weighed into 10 ml of 0.07 M disodium phosphate (Na_2HPO_4) and heated in an ultrasonic bath at 80 °C until completely dissolved. After cooling to room temperature, the samples were filtered through 0.45 μl syringe filters. 100 μl of each sample was injected through an autosampler. Standards and samples were measured twice to check reproducibility.

2.1.4. Sample preparation for Fourier-transform infrared (FT-IR) spectroscopy

Unfilled and filled hydrogels were freshly prepared as described above. Cylindrical sections of 1 cm diameter were cut from the main hydrogel blocks. Using a cutter, the cylindrical cutouts were manually cut into the thinnest possible slices. The hydrogel slices were placed on a non-stick surface and allowed to dry at room temperature for 3 days. Dried sample discs were stored at room temperature in an environment with low relative humidity prior to measurements.

2.1.5. Sample preparation for X-Ray Diffraction Analysis (XRD)

Unfilled and filled hydrogels were again freshly prepared as described above. The entire hydrogel blocks were then transferred to independent glass Petri dishes and stored in a laboratory freezer at −30 °C to pre-freeze for 4 h prior to lyophilization. After pre-freezing, the hydrogels in the Petri dishes were placed in a dry freezer (Christ Alpha 1–4) at −54 °C. The chamber was sealed, and a vacuum of 5×10^{-3} Torr was applied with an external pump. The hydrogels were kept under these conditions overnight to ensure complete lyophilization. After lyophilization, the hydrogels showed a significant reduction of their original volume due to the absence of water, while maintaining the original block shape. The observed structure showed high porosity, and slices of a few millimeters thickness were cut from the dried sample blocks and used for XRD measurements (Fig. 1). Powdered mesoporous silica particles and $CaCO_3$ powders were analyzed as received.

2.2. Rheometric characterization

All the experimental rheometric measurements were performed using an MCR 702e MultiDrive Space Rheometer (Anton Paar) with the necessary accessories, as described in the following sections.

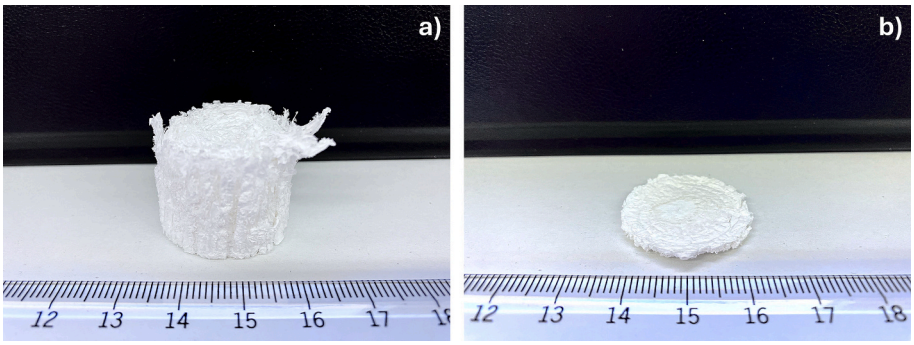

Fig. 1. a) Freeze-dried filled hydrogel and b) a cutout for the XRD experiments.

2.2.1. Gelation

The purpose of the gelation experiments was to monitor the growth of the viscoelastic moduli, G' and G'', up to their maximum plateau values, where G' is the storage or elastic modulus, and G'' is the loss or viscous modulus. Sample preparation was performed as described in Sec. 2.1.1, but with one exception: without the addition of the $CaCO_3$ dispersion and GDL solution. The temperature of the Alg/gellan solution was kept at 50 °C. To prepare fresh samples for each gelation kinetics experiment, 90 ml of polysaccharide solution was kept at 50 °C with stirring, and 5 ml of $CaCO_3$ dispersion and 5 ml of GDL solution were kept separately. A 9 ml aliquot of the polysaccharide solution was poured into the vial, and then 0.5 ml aliquots of both the $CaCO_3$ and GDL were added to trigger gelation. The mixture was stirred vigorously with a spoon. Afterward, enough of the mixture was added to the lower plate of the rheometer. The upper plate was quickly adjusted to the final gap position of 1 mm, and the measurement was started. Small amplitude oscillatory shear (SAOS) deformations were performed with a constant frequency of $\omega = 6.28$ rad/s and a constant strain amplitude of $\gamma = 0.1$ %. A 25 mm parallel plate with a rough surface was used to prevent wall slippage. The temperature was maintained at 50 °C for 30 min and then gradually decreased to 20 °C at a rate of 1 °C/min. The sample, which was already in a fully gelled state, was held at 20 °C for 15 min. The measurements were performed at room temperature without relative humidity control. The final curves are the result of averaging over three replicates with fresh sample, where the error bars correspond to the standard deviation.

2.2.2. Torsional - extensional mechanical tests

The samples were formed into cylinders with a length (L) of 40 mm and a diameter (D) of 5 mm and clamped in a CTD 180 temperature-humidity chamber (Anton Paar) (Fig. 2). To prevent the sample from slipping out of the clamp, the ends of the cylinder were covered with small rectangular pieces of a laboratory paper tower. The specimens were subjected to dynamic extensional and torsional loading. Due to the large L/D ratio, this technique allowed a high percentage of the hydrogel surface to be exposed to the environment, allowing water and heat exchange while the sample was deformed. The selected L/D ratio was large enough to obtain E' and E'' independent of L/D. This is a significant advantage over classical squeeze flow tests on hydrogels with parallel plates (Wingstrand et al., 2016). Besides, for cylindrical samples, there are no warping deformations due to torsion. Thus, there is no torque contribution due to warping and therefore no correction of the complex shear modulus was necessary (Dessi, 2016; Dessi et al., 2021; Diani & Gilormini, 2017; Kim et al., 2024; Müller-Pabel et al., 2022; Rodríguez-Agudo et al., 2023). The setup thus provided absolute values for shear (G', G'') and extensional modulus (E', E'') in a continuous measurement run. Temperature or humidity variations may cause changes in the original diameter of the cylindrical sample due to absorption or evaporation processes, possibly leading to inaccuracies in the estimation of viscoelastic moduli since changes in diameter cannot be tracked with the device. To overcome this problem, the sample was monitored in the chamber to account for any relevant changes in the specimen geometry during the measurement.

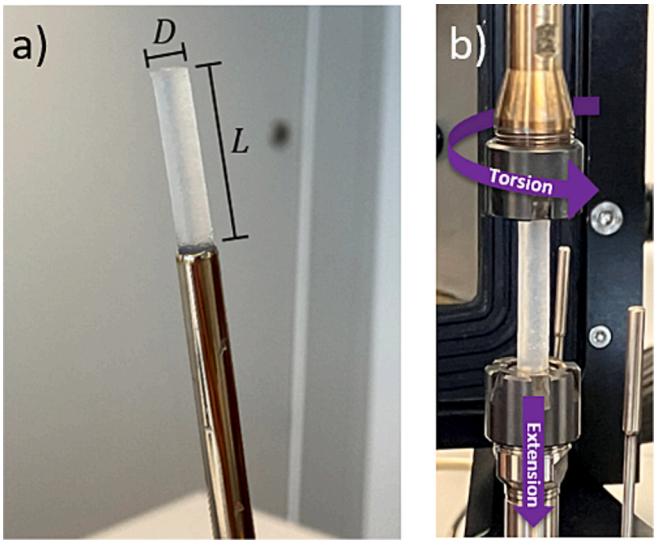

Fig. 2. a) Cut out of the hydrogel in a cylindrical shape. b) Clamped cylindrical sample in the DMA geometry. Purple arrows represent the different types of deformations applied to the hydrogel sample.

2.2.2.1. Amplitude sweeps. Amplitude sweep tests under shear and extensional deformations were performed independently. For both types of tests, a constant angular frequency of $\omega = 1$ rad/s was employed. For torsional tests, the values of the shear strain were selected between 0.01 and 1000 %. In the case of the extensional tests, extensional forces between 1 and 1000 mN were selected. The initial value for the extensional force was selected as small as 1 mN to ensure the measurement started well within the liner viscoelastic regime (LVR). The temperature was set at 30 °C, which is approximately the human skin temperature, and the relative humidity was set at 90 % to prevent rapid water loss from the hydrogel by evaporation. The final curves in Fig. 4 are the result of averaging over three replicates with fresh sample, where the error bars correspond to the standard deviation.

2.2.2.2. Frequency sweeps. Frequency sweeps were performed in torsion, immediately followed by the same frequency sweep in extension. The angular frequency varied from 100 to 1 rad/s. At each angular frequency, the cylindrical specimen was first subjected to torsion with a constant shear strain of 0.1 % and then to tensile stress with a constant strain force of 30 mN, resulting in strain amplitudes between 0.1 and 0.15 %, depending on the frequency applied. The amplitudes in both deformation modes were always within the LVR. The environmental

conditions were the same as for the amplitude sweeps described in Sec. 2.2.2.1. The final curves in Fig. 5 are the result of averaging over three or four replicates with fresh sample, where the error bars correspond to the standard deviation.

2.2.2.3. Temperature sweeps. The angular frequency was fixed at 6.28 rad/s, the selected strain amplitude was $\gamma = 0.1$ % for torsion, and a constant strain force of 30 mN was selected for the tensile mode. Four different temperatures were selected: 10, 20, 30, and 40 °C. The relative humidity was fixed at 90 %. At each temperature, the specimen was subjected first to torsion and then to tensile strain so that both the linear viscoelastic torsion and tensile strain moduli could be determined. For each data point in Fig. 6, which corresponds to a single temperature, a total of four points were measured and averaged during the same measurement run. The error bars, which are not visible on the graph because they are virtually negligible, correspond to the standard deviation.

2.2.2.4. Relative humidity sweeps. Again, the angular frequency was fixed at 6.28 rad/s, the strain amplitude was $\gamma = 0.1$ % for torsion, and a constant strain force of 30 mN was selected for the tensile mode. A ramp-down of the relative humidity was first applied from 90 to 30 % at a rate of 1 % per measurement point, and then a ramp-up was implemented from 30 to 90 %. The temperature was fixed at 30 °C. At each relative humidity, the specimen was subjected first to torsion and then to extension to determine the linear viscoelastic torsional and extensional dynamic moduli. The final curves in Fig. 8 are the result of averaging over three replicates with fresh sample, where the error bars correspond to the standard deviation.

2.2.2.5. Breaking rod tests. The breaking rod tests were performed in torsion with a continuous angular deformation rate of $\varphi = 1°/s$. The shear stress was determined for each angular deformation, and the test was terminated either by fracture of the cylindrical sample or by slippage. The specimen was monitored in the chamber, and the measurement was stopped manually after any of the above events were observed. The environmental conditions were the same as for the amplitude sweeps described in Sec. 2.2.2.1. Each curve in Fig. 9 represents a single measurement on a fresh sample, therefore error bars are not shown.

2.3. Molecular and structural characterization

The molecular weight distribution and the average molecular weight of the polysaccharides were determined by GPC, while the structural analysis of the hydrogels was performed by FT-IR and XRD measurements.

2.3.1. GPC

The molecular weight distribution and the average molecular weight of the polysaccharides using an LC 1260 Infinity with RID detection (Agilent). The columns used were SUPREMA_10µm - Pre-Column (8 × 50 mm) + SUPREMA Linear M_10µm (8 × 300 mm), both from Polymer Standards Services (PSS). The average molecular weight was obtained from two independent measurements on fresh sample. The error was taken as the standard deviation.

2.3.2. FT-IR

FT-IR measurements were performed at room temperature using a Lyza 7000 FT-IR spectrometer (Anton Paar) equipped with an IRIS single reflection diamond ATR (PIKE Technologies). Each spectrum shown in Fig. 10 is the resulting average of 24 scans. The standard deviation is negligible.

2.3.3. XRD

XRD measurements were performed on a D8 Advance (Bruker) equipped with a Lynxeye® position sensitive detector (PSD) in θ-θ geometry. A variable divergence slit and a 2.3° soller slit on the secondary side were used. The XRD data were acquired over a 2θ range of 5–85° 2θ at 0.5 s per 0.013°2θ step. This gave a total count time of 96 s per step using the PSD. The instrument used Cu anodes with Cu Kα1,2 radiation ($\lambda = 0.154018$ nm).

3. Results and discussion

3.1. Two-step gelation

The gelation test was carried out for the unfilled Alg/gellan gel using a parallel-plate geometry, as mentioned in Sec. 2.2.1. The experimental result is depicted in Fig. 3, showing a two-step gelation process (Li et al., 2020). The process describes two different gelation mechanisms associated with the two types of polymers involved. Here, Alg and gellan form independent continuous gel networks, which entangle each other. This mechanism corresponds, in fact, to the concept of interpenetrating polymeric networks applied to binary gels. The first gelation step was observed during the initial 1800 s (incubation time at 50 °C). Within this time interval, a significant increase of the viscoelastic moduli, *G'* and *G"*, was observed. This can be correlated with the separate crosslinking of Alg and gellan. In the subsequent cooling process, which lasted 1800 s and in which the temperature gradually lowered to 20 °C, the viscoelastic moduli finally reached a plateau value after another significant increase. This corresponds to a second gelation step, mainly related to further aggregation of gellan in conjunction with some strengthening of the Alg network. Eggbox formation by Ca^{2+} ions binding to Alg and Ca^{2+} screening of the negative charges of gellan molecules is a competitive process. In the first gelation step, the higher negative charge density of Alg may favor the binding of Ca^{2+} ions to Alg molecules. Although the corresponding measurement points in the very early gelation stage showed some fluctuations due to small torques of the rheometric signal, the crossover of *G'* and *G"* was observed to occur ~ 2 min after the start of the measurement (see the short-time region in Fig. 3).

In this work, GDL and $CaCO_3$ were added to the polymer solution for crosslinking. The mixture was then stirred, and a sufficient amount of sample was quickly added to the base plate of the rheometer geometry. The gelation time was prolonged by the specific selection of the crosslinker so that the crossover of the viscoelastic moduli could be recorded. Note that, when $CaCl_2$ or another fast crosslinker is used, the experimental setup must be adapted to capture the crossover of the viscoelastic moduli and to follow their subsequent evolution properly. For example, Besiri et al. (2020) reported the development of a customized

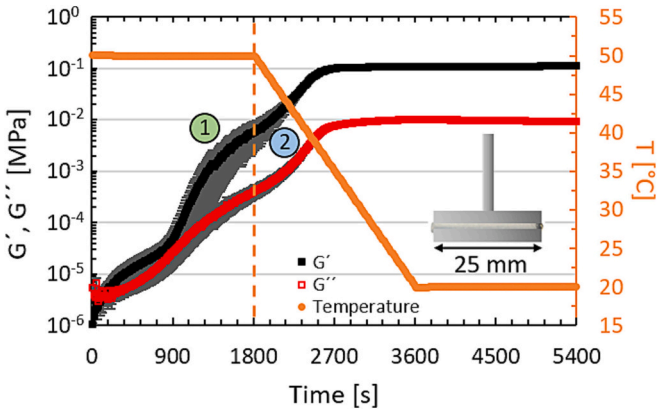

Fig. 3. The gelation curve for the unfilled Alg/gellan gel with a concentration ratio of 2:8. *G'* and *G"* are the viscoelastic moduli, and *T* is the temperature inside the humidity chamber. Number 1 in the green circle indicates the first phase of gelation during incubation at 50 °C. Number 2 in the blue circle refers to the second phase of gelation during the cooling process.

rheological experimental setup that allowed the rapid gelation of Alg and Ca^{2+} to be monitored in situ and in real-time, with the transition between G' and G'' observed as early as 5 s after the onset of the gelation reaction. In this custom-built setup, gelation is induced using a baseplate geometry with two tiny holes on the surface of the baseplate through which the crosslinker is brought into contact with the sample. A certain volume of crosslinker is injected into the cavity of the base plate using a connected syringe, and the additional volume is pushed into the cavity, which is completely prefilled with crosslinker and forces the same amount through the tiny holes into the sample. $CaCl_2$ is widely used as a crosslinker for Alg, but due to its high solubility in water, gelation occurs very quickly. One approach to slow gelation and gain more control over the gelation process is to use $CaCO_3$ due to its lower solubility in aqueous solutions. The addition of GDL lowers the pH and gradually dissociates Ca^{2+} from $CaCO_3$. The increase in free Ca^{2+} due to its release from $CaCO_3$ results in slower internal gel formation and a more homogeneous final microstructure. The implementation of this approach is well-suited for bio-printing or 3D printing.

3.2. Strain amplitude sweeps at constant temperature and relative humidity

The experiments were performed for the unfilled and filled hydrogels under constant temperature $T = 30$ °C and constant relative humidity $RH = 90$ %. The high humidity value was selected to bring the water desorption rate to a minimum during the experiment, subsequently reducing the impact of possible sample volume variations. Results are depicted in Fig. 4, where the shear and extensional moduli are presented as a function of the shear strain and the extensional strain, respectively. Data points are the result of an average of over three or more independent measurements. The error bars represent the standard deviation. In the case of the torsional tests, the sample was subjected to a varying strain amplitude, and, on the other hand, a varying extensional force was applied in the case of the extensional tests, as mentioned in Sec. 2.2.2.1.

In strain amplitude sweep tests in torsion (Fig. 4a), the three systems show an initial plateau value over a certain range of strain amplitudes, which delimits the conventional LVR. A drop from the plateau values of the storage moduli determines the end of the LVR. For the pure gellan gel (red squares), the LVR is restricted to a smaller strain amplitude when compared to the other two systems. This is related to the brittle and stiff character of the structure formed by the gellan polymer chains, which also results in larger moduli values associated with higher stresses. These higher stresses are directly related to the length of the gellan polymer chains, which are approximately 3 times longer than sodium alginate chains, as determined by GPC experiments. For the case of the unfilled and filled Alg/gellan gels (black squares and blue squares), the LVR ends at larger strain amplitudes. The Alg polymeric network introduces ductility and softness to the overall microstructure, postponing fracture and resulting in smaller moduli values. For the three systems, the storage modulus is approximately one order of magnitude larger than the loss modulus, indicating a predominant elastic character. The embedded silica particles make the hydrogel more brittle and thus slightly increase the torsional storage modulus. A stronger reinforcement of the mechanical properties of the filled hydrogel can be achieved, for instance, by crosslinking the particles with the matrix (Tallawi & Germann, 2020). In the tensile tests (Fig. 4b), the LVR is extended over a shorter interval of strain amplitudes. Again, the values of the extensional storage modulus for the pure gellan gel are larger than those corresponding to the other two systems, and the effect of the embedded particles is not significant when comparing the unfilled and filled Alg/gellan gels. As expected for isotropic materials, the absolute complex Young's modulus, $|E^*| = \sqrt{(E')^2 + (E'')^2}$, remains 2–3 times larger than the absolute complex shear modulus, $|G^*| = \sqrt{(G')^2 + (G'')^2}$, for unfilled materials over a wide range of deformations. This is also true for the filled Alg/gellan gels, indicating that the filler does not cause anisotropy in the mechanical properties of the sample. The absolute complex Poisson's ratio, $|\nu^*|$, can be defined as (Rodríguez-Agudo et al., 2023):

$$|\nu^*| = \sqrt{\frac{|E^*|^2}{4|G^*|^2} - \frac{|E^*|}{|G^*|}cos(\delta_E - \delta_G) + 1}\,, \tag{1}$$

where δ_G and δ_E are the phase shift angles for torsional and extensional measurements, respectively. Our aim for the amplitude sweeps is a qualitative comparison. The absolute complex Young's and shear moduli were obtained on two different samples, making it difficult to quantify the absolute complex Poisson's ratio with high precision (Rodríguez-Agudo et al., 2023). The pure gellan gel has an average value of 0.32 ± 0.03 in the LVR. This is well below the values for unfilled and filled Alg/gellan gels, which are 0.44 ± 0.06 and 0.42 ± 0.07, respectively. A lower absolute complex Poisson's ratio again indicates a less compliant and stiffer/brittle material compared to Alg/gellan. On the other hand, the low influence of fillers on the polymer network is again confirmed by a similar complex Poisson's ratio of filled and unfilled Alg/gellan. When both samples are subjected to the same extensional (or compressional) strain, ε, the results show that the pure gellan gel exhibits a greater change in volume than the Alg/gellan sample. This is

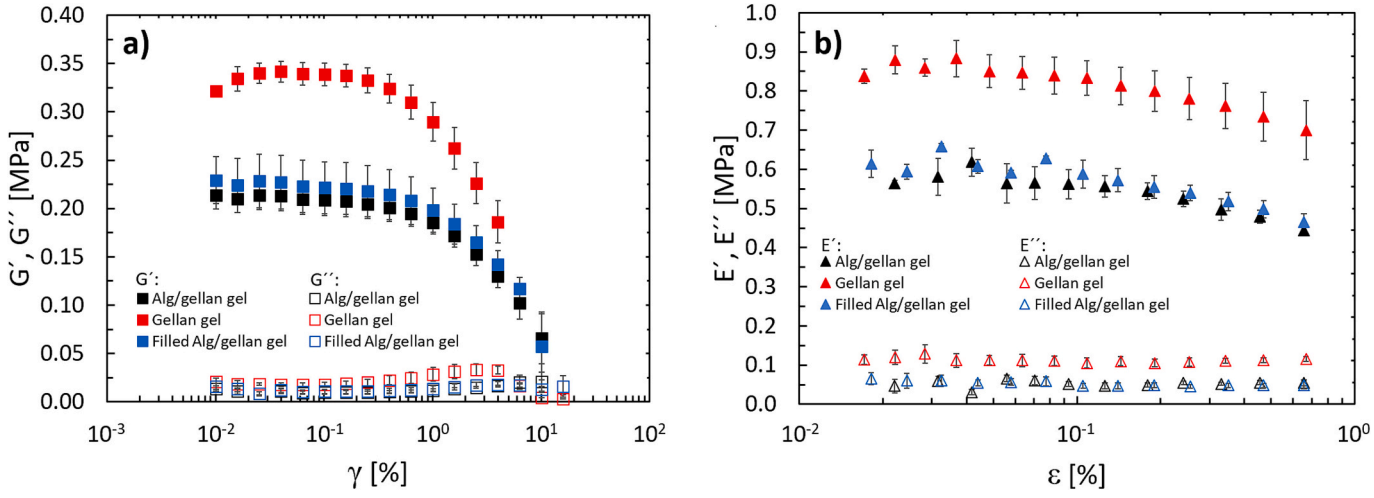

Fig. 4. Amplitude sweeps tests in a) torsion and b) extension for the unfilled and filled hydrogels. Shear (G', G'') and extensional (E', E'') moduli are presented as a function of the shear strain, γ, and the extensional strain, ε, respectively, for $T = 30$ °C and $RH = 90$ %.

also immediately apparent from the approximation $\Delta V/V \approx (1-2|\upsilon^*|)\varepsilon$ (Rodríguez-Agudo et al., 2023).

3.3. Frequency sweeps at constant temperature and relative humidity

Angular frequency tests were performed for the unfilled and filled hydrogels within the LVR at constant temperature $T = 30$ °C and relative humidity $RH = 90$ %. Again, the high relative humidity value was chosen to preserve the original sample size as much as possible by slowing the likely desorption of water. Experiments were conducted in torsion (Fig. 5a) and extension (Fig. 5b). As observed for interpenetrating network hydrogels that present a strong gel nature (Ng et al., 2023), they exhibit a reduced dependency of the viscoelastic properties on the angular frequency range studied, and an almost perfect power-law trend (dashed lines in Fig. 5).

It can be observed for both torsion and extension modes that, as in the case of strain sweeps, the pure gellan gel presents the highest response. The responses of the unfilled and filled Alg/gellan gels are very similar, whereas the filled hydrogel shows slightly higher elastic moduli values. Therefore, the presence of particles at the defined fraction 0.7 % (*w/v*) does not greatly influence the final mechanical properties as a function of frequency. Still, a small variation is observed, as in the case of strain sweeps (Fig. 4). The mesoporous silica particles used in the present work do not have a specific surface functionalization, which could then explain why changes in viscoelasticity are very small because of the low particle-polymer network interaction. The absolute complex Poisson's ratio was calculated for $\omega = 1$ rad/s, which is the angular frequency used in the amplitude sweep tests. Again, the lowest value is found for the gellan gel, 0.18 ± 0.02. This is followed by the filled and unfilled Alg/gellan gels, 0.33 ± 0.01 and 0.34 ± 0.06, respectively.

3.4. Temperature sweeps at constant relative humidity

Temperature sweeps were performed for the three different hydrogels at $RH = 60$ % and 90 %. The viscoelastic moduli were obtained at both fixed angular frequency and strain amplitude within the LVR. In Fig. 6a, storage moduli in torsion are shown for 90 % (filled squares) and 60 % (empty squares). At 90 %, it is readily observable that temperature does not play a role. A plausible explanation may be built on the fact that a very high *RH* is hindering material surface/environment water exchange due to quasi-water-saturated air. Results show an almost constant value for all the explored temperature values, where the pure gellan gel exhibits the highest elastic response, also observed in extension mode in Fig. 6b.

While the influence of temperature at $RH = 90$ % is negligible, the reduction to 60 % undoubtedly introduces a dependency on temperature. The overall drop is similar in both modes. For instance, at $T = 40$ °C in torsion, *G'* at the highest relative humidity is ~ 2.1 times larger than *G'* for the lowest relative humidity. This factor is ~ 2 in extension. The decrease in the storage modulus is also observed for the unfilled and filled Alg/gellan gels in extension mode for *E'*, with a dropping factor at $T = 40$ °C of ~ 1.5 for the unfilled hydrogel and of ~ 1.3 for the filled hydrogel. In torsion, the dropping factor at $T = 40$ °C for the unfilled hydrogel is ~ 1.6, larger than its counterpart for extension, which is ~ 1.4. In torsion, pure gellan gel shows a continuous decrease of the storage modulus, *G'*, with a dropping factor of ~ 1.3 between $T = 10$ °C and 40 °C. In extension, a continuous decrease of the extensional storage modulus, *E'*, with temperature is again observed for the gellan gel, with the same dropping factor of ~ 1.3. In the case of the unfilled/filled Alg/gellan gels, the dropping factors are similar for both systems in torsion (~1.4) and extension (~1.3).

3.5. Relative humidity sweeps at constant temperature

Relative humidity sweeps (RHS) were performed at a fixed angular frequency and at a fixed strain amplitude within the LVR for the three systems. As described in Sec. 2.2.2.4, relative humidity varied from 90 to 30 % and then from 30 to 90 % during the same experiment. The temperature is fixed at 30 °C.

As mentioned in Sec. 2.2.2, environmental conditions like temperature and relative humidity could affect the overall mechanical response of the hydrogel samples due to their effect on the sample's shape during the experiments through water desorption. Therefore, the cylindrical sample was monitored during each experimental test to account for possible shape changes. In Fig. 7a, the relative change of the sample's diameter is presented for different experiments over the test time. For clarity, the three hydrogels are compared only in the case of the relative humidity sweeps; for the strain sweeps (SS) and temperature sweeps (TS), only the filled Alg/gellan and the pure gellan gels are presented. We found that the diameter fluctuations during SS (green symbols) and TS (purple symbols) sweeps remained between −1.6 % and 1.6 %, approximately. Here, it is important to note that the relative humidity was fixed at 90 %. In contrast, diameter fluctuations are larger in the case of the RHS and especially relevant during the second part of the *RH* cycle, from 30 to 90 % (yellow symbols). Gellan gel presents the smallest diameter variations with a maximum of 3.9 % at the end of the experiment, followed by the filled Alg/gellan gel with a maximum of 6.25 %, and finally, the unfilled Alg/gellan gel with a maximum of 7.5 %. Interestingly, a rapid and earlier increase in the diameter variation is visible for the unfilled hydrogel compared to the filled hydrogel and the

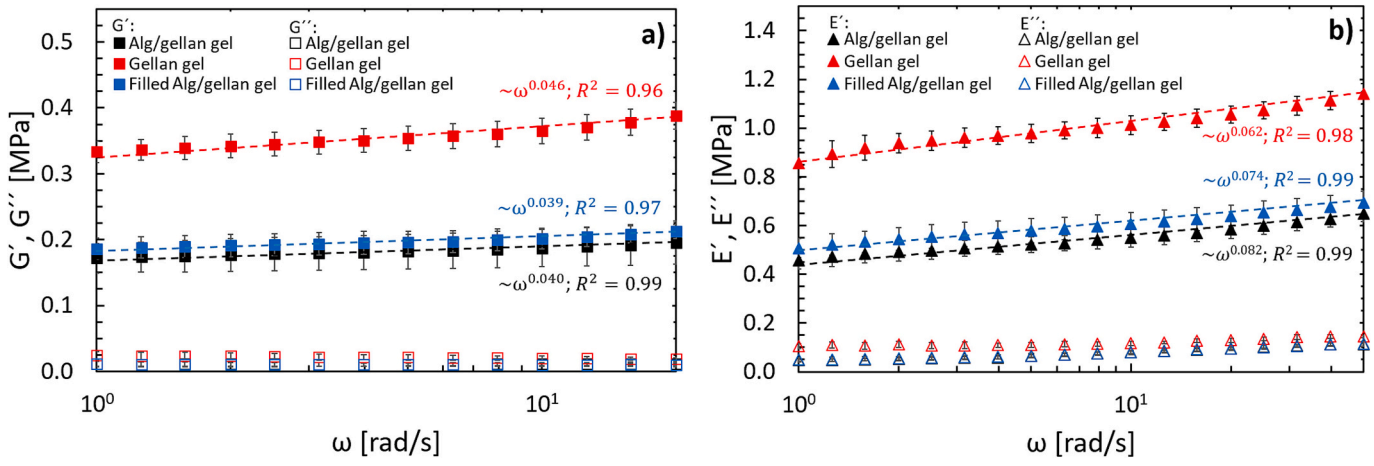

Fig. 5. Angular frequency sweep tests in a) torsion and b) extension for the unfilled and filled hydrogels. Shear (*G'*, *G"*) and extensional (*E'*, *E"*) moduli are presented as a function of the angular frequency sweep, ω, for $T = 30$ °C and $RH = 90$ %. Dashed lines indicate a power-law fitting for the torsional and extensional elastic parts.

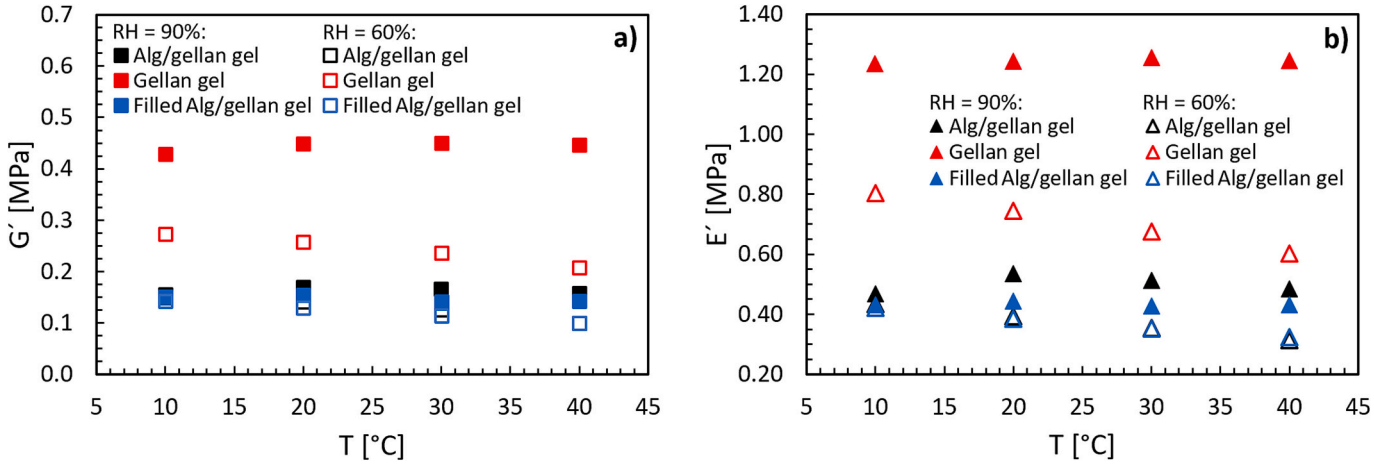

Fig. 6. Temperature sweep tests for four different temperatures: 10, 20, 30, and 40 °C, at two different relative humidity, $RH = 60$ % and 90 %. Experiments were performed for the unfilled and filled hydrogels. Storage moduli are presented as a function of temperature for $RH = 60$ % (empty squares) and 90 % (filled squares) in a) torsion and b) extension.

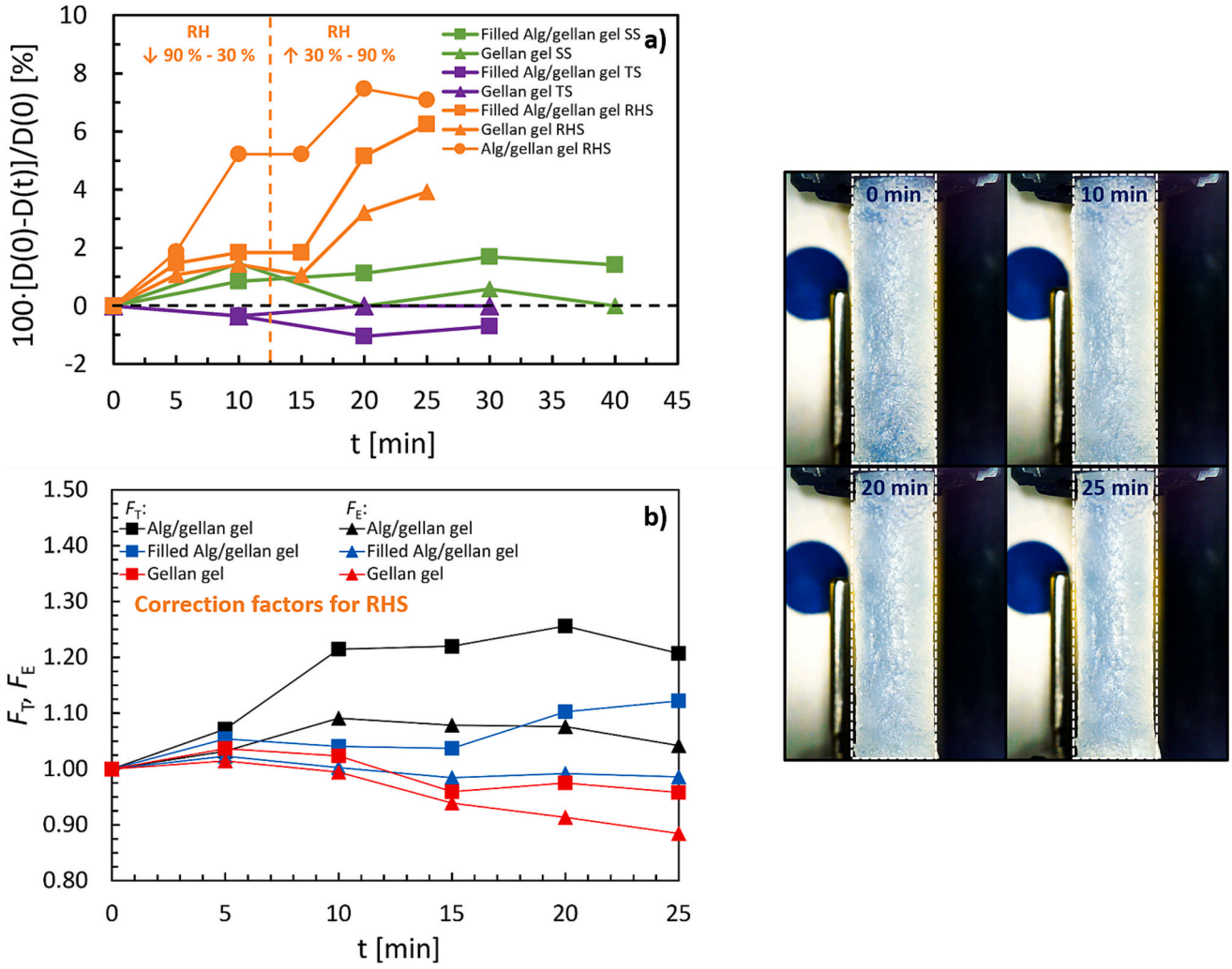

Fig. 7. Relative variation of the sample's diameter as a function of the test time. D (0) and D (t) are the diameters at the beginning of the experiment and at test time t, respectively, are presented in a). Three different tests are shown: green symbols are SS at $RH = 90$ % and $T = 30$ °C, purple symbols are TS at $RH = 90$ %, and orange symbols are RHS at $T = 30$ °C. Filled hydrogel (squares) and pure gellan gel (triangles) were compared for the three tests. Unfilled hydrogel (circles) is compared to the other systems only for RHS. The vertical dashed line marks the end of the first part of the RH cycle and the beginning of its second part. Correction factors in torsion, F_T, and in extension, F_E, obtained for the storage moduli of the different hydrogels during the first 25 min are shown in b). The images in c), d), e) and f) show the time evolution of the sample diameter of the Alg/gellan gel during an RHS test for different times during the experiment.

pure gellan gel.

For cylindrical specimens, the complex viscoelastic moduli are related to the specimen dimensions by the following expressions (Rodríguez-Agudo et al., 2023):

$$|G^*(t)| = \frac{M}{\varphi} \bullet \frac{32L(t)}{\pi D(t)^4}, |E^*(t)| = \frac{F}{s} \bullet \frac{4L(t)}{\pi D(t)^2}, \quad (2)$$

where M is the torque, φ is the deflection angle, F is the applied force, s is the displacement, and $L(t)$ and $D(t)$ are the length and the diameter at test time t of the cylinder, respectively. The dimensions of the cylindrical specimen are fixed at the beginning of the experiment, so the estimated viscoelastic moduli are based on these dimensions. If the length and diameter of the specimen remain approximately constant throughout the experiment, the preset dimensions are valid. However, if significant changes occur, as in the case of the RHS, correction factors for the viscoelastic moduli in torsion, F_T, and in extension, F_E, must be considered:

$$F_T(t) = \frac{|G^*_{corrected}|}{|G^*_{uncorrected}|} = \frac{D_0^4}{D(t)^4} \bullet \frac{L(t)}{L_0}, \text{ and} \quad (3)$$

$$F_E(t) = \frac{|E^*_{corrected}|}{|E^*_{uncorrected}|} = \frac{D_0^2}{D(t)^2} \bullet \frac{L(t)}{L_0}, \quad (4)$$

respectively. Here, L_0, and D_0 refer to the preset or initial length and diameter, respectively, and $L(t)$, and $D(t)$ are the actual length and diameter at instant t, respectively. It is important to notice that length is measured by the rheometer during the experiment. For simplicity, the viscoelastic modulus correction was implemented only for the storage modulus, considering the viscous part to be negligible compared to its elastic counterpart. This consideration leads to the following approximations $|G'| \cong |G^*|$, and $|E'| \cong |E^*|$. The correction factors shown in Fig. 7b correspond to discrete measurements taken every 5 min. A linear interpolation for each 5-min interval was considered to estimate the correction factors associated with the measured storage moduli at each time point.

The uncorrected RHS results are shown in Fig. 8a and c for torsion and extension, respectively. The corrected and uncorrected storage moduli are compared for torsion and extension in Fig. 8b and d, respectively. The corrected storage moduli are higher than the uncorrected ones because the correction factors F_T, and F_E are greater than 1 for each relative humidity value, except in the case of gellan gel where the correction factors are less than 1 during the second part of the relative humidity cycle. During the first part of the sweep cycle, where the relative humidity decreased from 90 % to 30 %, the three hydrogels experienced a continuous decrease in diameter in both torsional and extensional modes. The corresponding dropping factors for the uncorrected and corrected storage moduli are shown in Table 1. The dropping factor is calculated as the ratio between the initial and final values of the storage moduli for each cycle and mode. For the uncorrected moduli, within the first cycle, the Alg/gellan gel is the one that experiences the greatest reduction in both torsional and extensional modes, with dropping factors of ~1.70 and ~ 1.66, respectively. During the second part of the cycle, a similar reduction is observed for all systems, which is

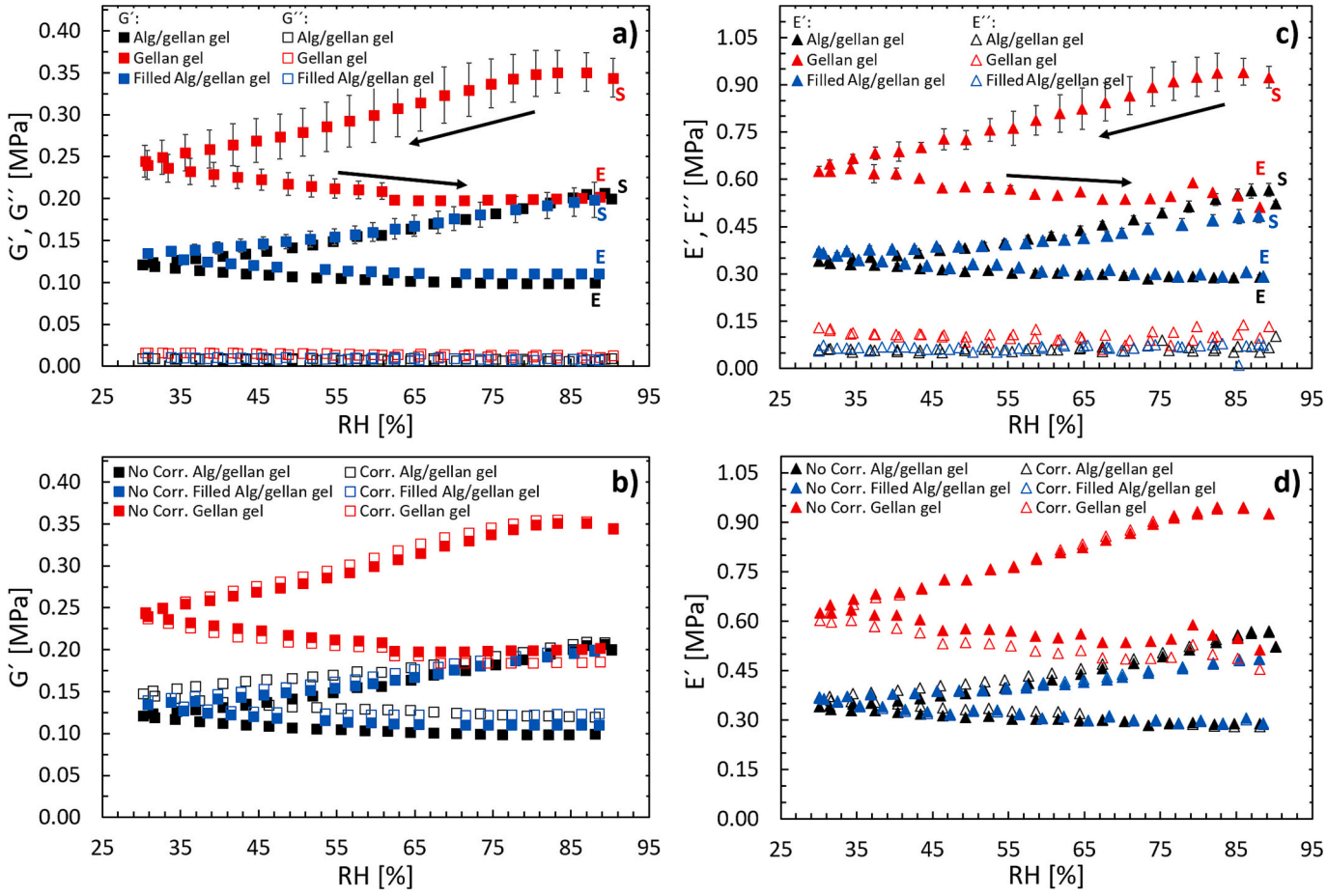

Fig. 8. Relative humidity sweeps at a constant temperature of 30 °C for unfilled and filled hydrogels. Uncorrected viscoelastic moduli are shown as a function of *RH* in a) torsion and c) extension. Corrected and uncorrected storage modulus comparisons are given in b) and d) for torsion and extension, respectively. Black arrows indicate the direction of the RHS, which runs over two intervals: from 90 to 30 % first and then from 30 to 90 %. Letters S and E refer to the start and the end of the RHS, respectively. Error bars are not shown in b) and d) for clarity.

Table 1
Dropping factors in torsion and extension modes for the full RHS cycle and for the first and second parts of the full RHS cycle for uncorrected (left) and corrected (right) storage moduli.

Dropping factors for uncorrected storage moduli				Dropping factors for corrected storage moduli			
Mode	**90 % → 30 % (full cycle)**			**Mode**	**90 % → 30 % (full cycle)**		
	Alg/gellan gel	Gellan gel	Filled Alg/gellan gel		Alg/gellan gel	Gellan gel	Filled Alg/gellan gel
Torsion	2.08	1.75	1.80	Torsion	1.74	1.91	1.61
Extension	1.95	1.71	1.67	Extension	2.03	1.94	1.69
	90 % → 30 % (first part of cycle)				**90 % → 30 % (first part of cycle)**		
	Alg/gellan gel	Gellan gel	Filled Alg/gellan gel		Alg/gellan gel	Gellan gel	Filled Alg/gellan gel
Torsion	1.70	1.44	1.50	Torsion	1.41	1.45	1.43
Extension	1.66	1.51	1.31	Extension	1.53	1.57	1.34
	90 % → 30 % (second part of cycle)				**90 % → 30 % (second part of cycle)**		
	Alg/gellan gel	Gellan gel	Filled Alg/gellan gel		Alg/gellan gel	Gellan gel	Filled Alg/gellan gel
Torsion	1.22	1.21	1.22	Torsion	1.17	1.28	1.13
Extension	1.17	1.14	1.26	Extension	1.29	1.24	1.27

stronger in torsional mode for the unfilled and filled Alg/gellan gels. Considering the dropping factor for the full cycle of relative humidity sweep (Table 1), the most affected mode is torsion, and the largest decrease in elasticity is experienced by the Alg/gellan gel, followed by the filled Alg/gellan gel, and finally by the pure gellan gel. In comparison to the uncorrected moduli, the corrected storage moduli show smaller decreases for the unfilled and filled Alg/gellan gels in torsion. In extension, however, the reduction is more pronounced. In the case of gellan gel, the decrease is greater in both torsion and extension compared to the uncorrected values. This means that a change in elasticity due to changes in specimen shape becomes more apparent after correction. An overall decrease in elasticity is observed for extension. Interestingly, the absolute values of the extensional storage moduli suffer a smaller change when corrected in comparison to their torsional counterparts. This can be observed in Fig. 8b and d.

3.6. Breaking rod tests at constant temperature and humidity

Breaking rod tests were performed for the three different hydrogels at constant $RH = 90$ % and $T = 30$ °C in torsion mode under a continuous angular deformation rate of $\varphi = 1°/s$. The hydrogel's high surface moisture induced early slippage in the clamping locations during sample twisting. Therefore, small cuts of soaking paper were attached to the hydrogel cylinder extremes to increase friction between the geometry and the sample to improve clamping (Fig. 9d and e). The three systems showed a similar pseudoplastic behavior before rod breaking or

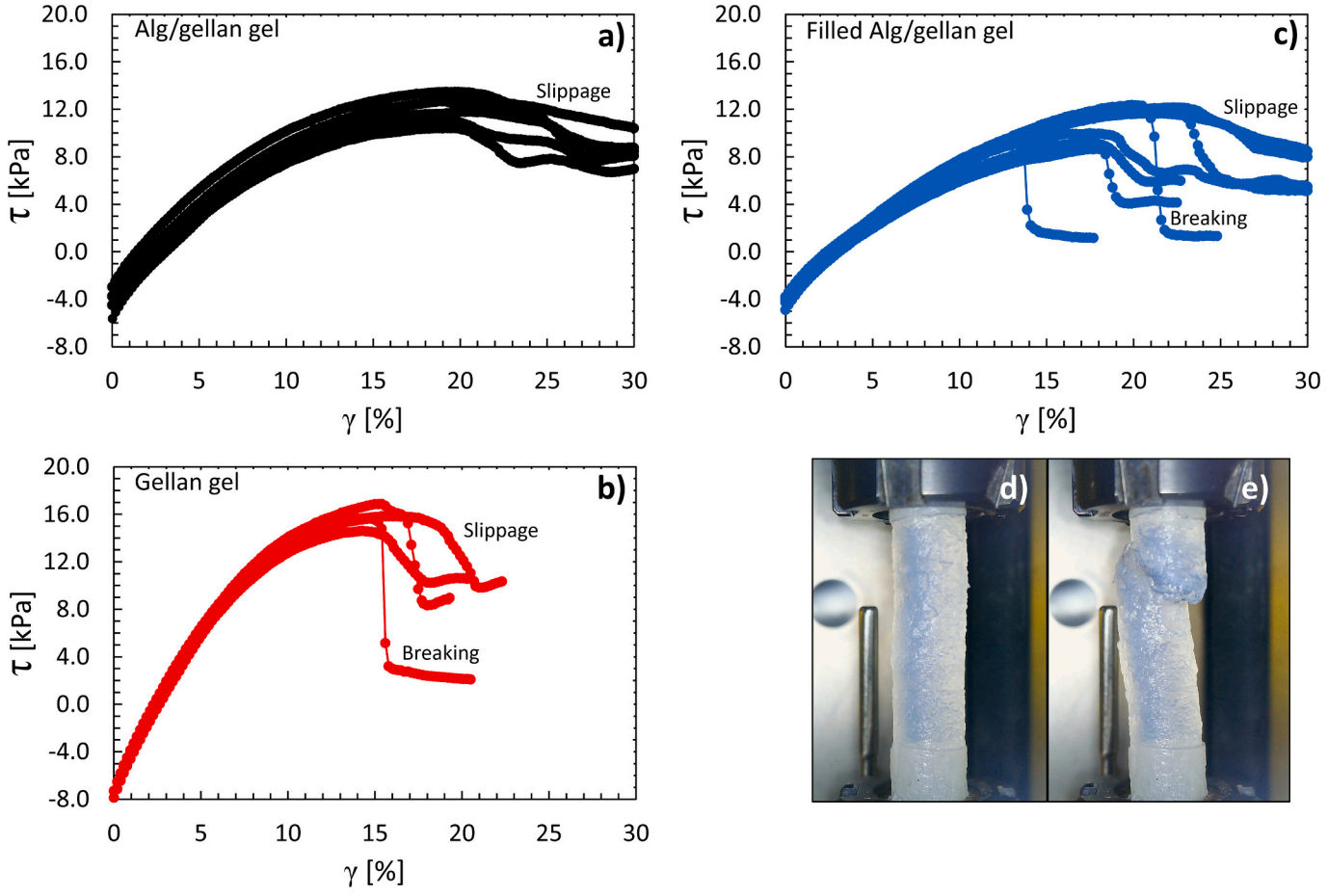

Fig. 9. Breaking rod tests in torsion for a) unfilled Alg/gellan gel, b) pure gellan gel, and c) filled Alg/gellan gel are presented. Shear stress, τ, is plotted versus shear strain, γ. Pictures of a cylindrical sample of the pure gellan gel before and after the breaking are shown in d) and e), respectively.

slippage. The main differences are observed in shear stress maxima and their associated strains. For unfilled and filled Alg/gellan gels, Fig. 9a and c, respectively, maximum shear stresses are between 8 and 12 kPa and are reached at $\gamma \sim 20$ %. The maximum shear stress corresponding to the pure gellan gel is, however, between 14 kPa and 17 kPa and is reached at $\gamma \sim 15$ % (Fig. 9b).

After reaching the maximum shear stress, the hydrogels undergo breaking or slippage, where the latest originates from the water expelled through the cylinder surface due to applied deformation (Banerjee & Ganguly, 2019; Zhang et al., 2022). Water coming out from the hydrogel wets the surface in excess, reducing friction between the sample and the clamps and then inducing slippage. This is reflected in the smoother decay of the shear stress. However, this phenomenon does not happen with the same frequency for the three hydrogels. The unfilled Alg/gellan gel always presents slippage (Fig. 9a), meaning that the amount of expelled water is large. In the case of the pure gellan gel (Fig. 9b), approximately half of the events correspond to slippage and the other half to breaking. This may be related to the higher brittleness of the gellan gel compared to the alginate gel and a possible barrier to water diffusion due to the internal polymer network. Finally, the filled Alg/gellan gel also shows both breaking and slippage (Fig. 9c). Here, particles seem to be hindering water diffusion, then reducing the amount of water expelled. Therefore, this would prevent slippage occasionally. The capacity of retaining water regarding microstructure nature/composition is in accordance with water loss during relative humidity sweeps (Fig. 8), where the diameter variations are smaller for the filled Alg/gellan and the pure gellan gels compared to the unfilled Alg/gellan gel. A plausible reason to explain the occasional slippage for the filled hydrogel and the pure gellan gel can be related to the clamping of the sample: anchoring force at both sample ends could vary, which would determine how tightly the sample is clamped. During breaking rod tests, applied torsional stresses are high, especially when approaching the stress limit. These high torsional stresses compete with the anchoring force, where the latest can occasionally be overcome by the first, leading to slippage. This can also explain why slippage is not observed for amplitude and frequency sweep tests: applied stresses are much smaller compared to the anchoring force.

3.7. GPC

The estimated average molecular weight for Alg is $(6.105 \pm 0.007) \times 10^5$ Da, which is in the same order of magnitude as a previously reported value of 1.57×10^5 Da (Topuz et al., 2012). In the case of gellan gum, the estimated average molecular weight is $(1.83 \pm 0.07) \times 10^6$ Da, which is in accordance with what was published in the work of Chen et al. (2017).

3.8. FT-IR

FT-IR spectra for the unfilled and filled dried hydrogels are shown in Fig. 10. In the case of the Alg/gellan and gellan gels, the pattern peaks can be clearly identified as peaks coming from gellan gum (Meera Naachiyar et al., 2021), which is the predominant component in the hydrogels besides water. The presence of Alg in Alg/gellan gels does not induce either wavenumber shifts or the appearance of new relevant peaks. This suggests that there is no significant interaction between the Alg and gellan networks. The presence of silica particles in the filled Alg/gellan gel can be observed in the characteristic FT-IR peak of SiO_2 (Ioniţă et al., 2022). The corresponding stretching bands of the peaks for each component of the hydrogel are shown in Table 2.

3.9. XRD

The XRD diffractograms for the unfilled and filled lyophilized hydrogels and for the $CaCO_3$ and silica powders are shown in Fig. 11. The sharp peaks observed in the patterns of the three samples, with 2θ between 29.4° and 65.7°, correspond to the diffraction pattern of $CaCO_3$ with its dominant peak at $2\theta \approx 29.4°$. This indicates the crystalline nature of the $CaCO_3$ structure, comparable to previously reported results (Li et al., 2020). Note that no new crystalline structures are formed. In the case of the Alg/gellan gel and the pure gellan gel samples, the broader peaks between 5.5° and 21.5° correspond to the XRD pattern of gellan gum, which is in very good agreement with previous publications (Meera Naachiyar et al., 2021). In the case of the filled Alg/gellan gel, there is a broader peak located at $2\theta \approx 23°$ due to the presence of SiO_2 (silica particles), which is consistent with the pure SiO_2 XRD pattern measured in this work and reported in the literature (Sidney Santana et al., 2021).

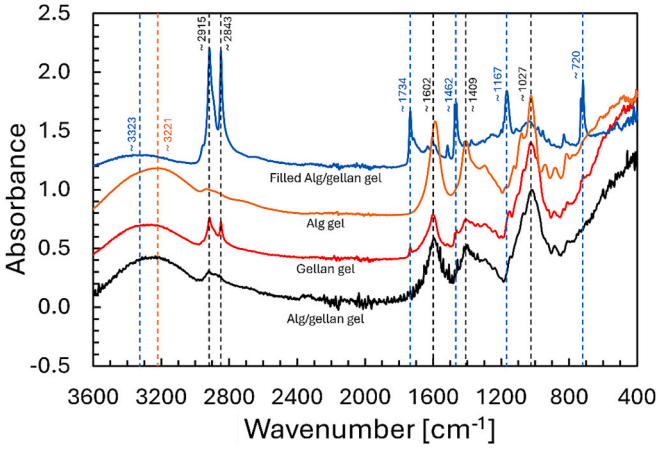

Fig. 10. Absorption FT-IR patterns of the filled and unfilled dried hydrogels are shown. Relevant pattern peaks are identified by the values of their corresponding wave numbers. Dashed lines in black indicate common relevant peaks. Dashed lines in blue correspond to peaks that only appear for the filled Alg/gellan gel. Each spectrum was normalized by its highest peak value and displaced along the Y-axis to improve the viewing.

Table 2
Stretching band assignments for FT-IR pattern peaks shown in Fig. 10.

Wavenumber [cm^{-1}]	Material	Stretching band	Reference
720	Silica	Si-O-Si	Ioniţă et al., 2022
1027	Alginate & Gellan	C-O	Modrogan et al., 2020; Sarker et al., 2014; Panday et al., 2023; Wang et al., 2021
1167	Silica	Si-O-Si	Ioniţă et al., 2022
1409	Alginate & Gellan	Symmetric carboxyl group	Modrogan et al., 2020; Sarker et al., 2014; Panday et al., 2023 Wang et al., 2021
1462			
1602	Alginate & Gellan	Asymmetric carboxyl group	Modrogan et al., 2020; Sarker et al., 2014; Panday et al., 2023; Wang et al., 2021
1734	Oxidized Gellan gum	C=O	Wang et al., 2021
2843–2915	Alginate & Gellan	C-H	Panday et al., 2023
3221–3323	Alginate & Gellan	O-H	Modrogan et al., 2020; Panday et al., 2023

4. Conclusions

In this work, we have presented a systematic study of the mechanical properties of three different model hydrogels by implementing a combined axial-torsional rheometric approach. We have shown that this

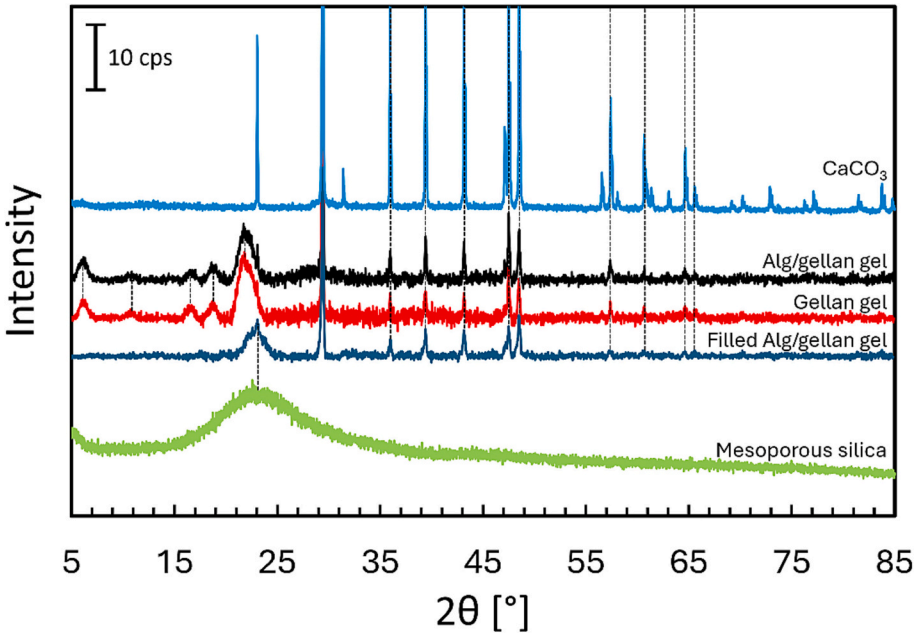

Fig. 11. Background subtracted XRD patterns for the unfilled and filled lyophilized hydrogels, pure $CaCO_3$ and pure mesoporous silica particles are shown. The different dashed lines indicate the matching peaks between different diffractograms. The scale bar indicates 10 counts per second (cps).

approach can be extended to softer materials such as hydrogels and that absolute values of the shear (*G', G"*) and extensional (*E', E"*) moduli can be measured in a continuous measurement run. We used cylindrical samples with a large *L/D* ratio, providing *E'* and *E"* independent of *L/D*, which turns into a considerable advantage over classical squeeze flow tests on hydrogels using parallel plates. Besides, the use of cylindrical samples prevents using further warping correction factors for obtaining *G'* and *G"*. On the other hand, the sample's cylindrical shape provided a larger hydrogel surface exposed to the environment, facilitating water and heat exchanges. This allowed us to study in detail the effect of temperature and relative humidity on the material mechanical properties. Relative humidity turned out to be the primary factor affecting hydrogel mechanical properties, whereas only at low/medium relative humidity values is the participation of temperature triggered. Importantly, a correction for viscoelastic moduli was necessary, since variations in relative humidity affected the dimensions of the samples. The inclusion of silica particles showed only a small improvement in the mechanical properties. More importantly, the presence of fillers seemed to affect water diffusion towards the hydrogel surface, consequently reducing water loss due to environmental and external stress factors. A future study could be the selective crosslinking of surface functionalized particles with gellan gum, alginate, or both biopolymers for reinforcement.

CRediT authorship contribution statement

Juan Pablo Segovia-Gutiérrez: Writing – original draft, Methodology, Investigation, Formal analysis, Data curation, Conceptualization. **José Alberto Rodríguez Agudo:** Writing – review & editing, Writing – original draft, Methodology, Investigation, Formal analysis, Data curation, Conceptualization. **Nicolas Binder:** Writing – original draft, Investigation, Formal analysis, Data curation. **Peter Georg Weidler:** Writing – review & editing, Writing – original draft, Investigation, Formal analysis, Data curation, Conceptualization. **Frank Kirschhöfer:** Investigation, Formal analysis, Data curation. **Claudia Fink-Straube:** Writing – review & editing, Writing – original draft, Investigation, Formal analysis, Data curation, Conceptualization. **Jürgen Utz:** Writing – review & editing, Supervision, Resources. **Natalie Germann:** Writing – review & editing, Supervision, Resources, Project administration, Methodology, Investigation, Conceptualization.

Declaration of competing interest

The authors declare the following financial interests/personal relationships which may be considered as potential competing interests: There is no conflict of interest to report. If there are other authors, they declare that they have no known competing financial interests or personal relationships that could have appeared to influence the work reported in this paper.

Data availability

Data will be made available on request.

References

Ahmed, E. M. (2015). Hydrogel: Preparation, characterization, and applications: A review. *Journal of Advanced Materials, 6*, 105–121.
Amiri, A., Baniassadi, M., Bayat, M. R., & Baghani, M. (2023). Transient swelling of cylindrical hydrogels under coupled extension-torsion: Analytical and 3D FEM solutions. *Journal of Intelligent Material Systems and Structures, 34*, 415–424.
Anjum, N., Joyal, N., Iroegbu, J., Li, D., & Shen, C. (2021). Humidity-modulated properties of hydrogel polymer electrolytes for flexible supercapacitors. *Journal of Power Sources, 499*, Article 229962.
Banerjee, A., & Ganguly, S. (2019). Mechanical behaviour of alginate film with embedded voids under compression-decompression cycles. *Scientific Reports, 9*, 13193.
Besiri, I. N., Goudoulas, T. B., & Germann, N. (2020). Custom-made setup for in situ real-time rheological characterization of fast alginate Ca^{2+} gelation. *Carbohydrate Polymers, 246*, 0144–8617.
Brumberg, V., Astrelina, T., Malivanova, T., & Samoilov, A. (2021). Modern wound dressings: Hydrogel dressings. *Biomedicines, 9*, 1235.
Chen, Q., Ma, H., Yuan, Y., Han, X., Zhu, J., & Zhang, H. (2017). Rheological behavior of high acyl gellan gum solution at gel point. *International Journal of Food Properties, 20*, S2332–S2341.
Chervinskii, S., Issah, I., Lahikainen, M., Rashed, A. R., Kuntze, K., Priimagi, A., & Caglayan, H. (2021). Humidity- and temperature-tunable metal–hydrogel–metal reflective filters. *Applied Materials & Interfaces, 13*, 50564–50572.
Dessi, C. (2016). Analysis of dynamic mechanical response in torsion. *Journal of Rheology, 60*(2), 275–287.
Dessi, C., Coppola, S., & Vlassopoulos, D. (2021). Dynamic mechanical analysis with torsional rectangular geometry: A critical assessment of constrained warping models. *Journal of Rheology, 65*(3), 325–335.

Diani, J., & Gilormini, P. (2017). On necessary precautions when measuring solid polymer linear viscoelasticity with dynamic analysis in torsion. *Polymer Testing, 63*, 275–280.
Dong, B., Yu, D., & Liu, W. (2023). Ultrastretchable, repairable and highly sensitive xanthan collagen nanosilver hydrogel for wide temperature flexible sensing. *Chemical Engineering Journal, 470*, Article 144385.
Dutta, T., Chaturvedi, P., Llamas-Garro, I., Velázquez-González, J. S., Dubey, R., & Mishra, S. K. (2024). Smart materials for flexible electronics and devices: Hydrogel. *Royal Society of Chemistry Advances, 14*, 12984.
Ed-Daoui, A., & Snabre, P. (2021). Poroviscoelasticity and compression-softening of agarose hydrogels. *Rheologica Acta, 60*, 327–351.
França, C. G., Plaza, T., Naveas, N., Santana, M. H. A., Manso-Silván, M., Recio, G., & Hernandez-Montelongo, J. (2021). Nanoporous silicon microparticles embedded into oxidized hyaluronic acid/adipic acid dihydrazide hydrogel for enhanced controlled drug delivery. *Microporous and Mesoporous Materials, 310*, Article 110634.
Goudoulas, T. B., & Germann, N. (2019). Nonlinear rheological behaviour of gelatin gels: In situ gels and individual gel layers filled with hard particles. *Journal of Colloid and Interface Science, 556*, 1–11.
Hazur, J., Detsch, R., Karakaya, E., Kaschta, J., Teßmar, J., Schneidereit, D., … Boccaccini, A. R. (2020). Improving alginate printability for biofabrication: Establishment of a universal and homogeneous pre-crosslinking technique. *Biofabrication, 12*, Article 045004.
Hu, X., & Qu, S. (2019). Inclusion size effect on mechanical properties of particle hydrogel composite. *Acta Mechanica Solida Sinica, 32*, 643–651.
Ioniță, S., Lincu, D., Mitran, R.-A., Ziko, L., Sedky, N. K., Deaconu, M., … Berger, D. (2022). Resveratrol encapsulation and release from pristine and functionalized mesoporous silica carriers. *Pharmaceutics, 14*, 203.
Jridi, M., Bardaa, S., Moalla, D., Rebaii, T., Souissi, N., Sahnoun, Z., & Nasri, M. (2015). Microstructure, rheological and wound healing properties of collagen-based gel from cuttlefish skin. *International Journal of Biological Macromolecules, 77*, 369–374.
Kim, Y. S., Rodríguez-Agudo, J. A., Wistuba, M. P., Büchner, J., & Schäffler, M. (2024). Determination of complex Poisson's ratio of asphalt binders using torsion-tension tests in a dynamic shear rheometer. *Road Materials and Pavement Design, 25*, 1–23.
Li, A., Gong, T., Yang, X., & Guo, Y. (2020). Interpenetrating network gels with tunable physical properties: Glucono-δ-lactone induced gelation of mixed Alg/gellan sol systems. *International Journal of Biological Macromolecules, 151*, 257–267.
Mayer, S., Tallawi, M., De Luca, I., Calarco, A., Reinhardt, N., Gray, L. A., … Germann, N. (2021). Antimicrobial and physicochemical characterization of 2,3 dialdehyde cellulose-based wound dressing systems. *Carbohydrate Polymers, 272*, Article 118506.
Meera Naachiyar, R., Ragam, M., Selvasekarapandian, S., Vengadesh Krishna, M., & Buvaneshwari, P. (2021). Development of biopolymer electrolyte membrane using Gellan gum biopolymer incorporated with NH4SCN for electro-chemical application. *Ionics, 27*, 3415–3429.
Modrogan, C., Pandele, A. M., Bobirică, C., Dobrotă, D., Dăncilă, A. M., Gârleanu, G., … C., Gârleanu, D., & Orbeci, C.. (2020). Synthesis, characterization and sorption capacity examination for novel hydrogel composite based on gellan gum and graphene oxide (GG/GO). *Polymers, 12*, 1182.
Mollica, F., Larobina, D., & Ambrosio, L. (2012). Combined extension and torsion of a swollen cylinder in unsteady conditions for the mechanical characterization of a hydrogel: An application of the continuum theory of mixtures. *International Journal of Engineering Science, 57*, 90–101.
Mori, M., Almeida, P. V., Cola, M., Anselmi, G., Mäkilä, E., Correia, A., … Santos, H. A. (2014). In vitro assessment of biopolymer-modified porous silicon microparticles for wound healing applications. *European Journal of Pharmaceutics and Biopharmaceutics, 88*, 635–642.
Müller-Pabel, M., Rodríguez-Agudo, J. A., & Gude, M. (2022). Measuring and understanding cure-dependent viscoelastic properties of epoxy resin: A review. *Polymer Testing, 114*, Article 107701.
Ng, J. Y., Yu, P., Murali, D. M., Liu, Y.-S., Gokhale, R., & Ee, P. L. R. (2023). The influence of pregelatinized starch on rheology of a gellan-collagen IPN hydrogel for 3D bioprinting. *Chemical Engineering Research and Design, 192*, 477–486.
Panday, A., Yadav, H., Patel, J., Paliwal, R., & Maiti, S. (2023). Calcium silicate-reinforced pH-sensitive alginate-gellan gum composite hydrogels for prolonged drug delivery. *Journal of Applied Polymer Science, 140*, Article e54392.
Rodríguez-Agudo, J. A., Haeberle, J., Müller-Pabel, M., Troiss, A., Shetty, A., Kaschta, J., & Giehl, C. (2023). Characterization of the temperature and frequency dependency of the complex Poisson's ratio using a novel combined torsional-axial rheometer. *Journal of Rheology, 67*(6), 1221–1250.
Sarker, B., Papageorgiou, D. G., Silva, R., Zehnder, T., Gul-E-Noor, F., Bertmer, M., … Boccaccini, A. R. (2014). Fabrication of alginate-gelatin crosslinked hydrogel microcapsules and evaluation of the microstructure and physico-chemical properties. *Journal of Materials Chemistry B, 2*, 1470–1482.
Sidney Santana, C., Freire Bonfim, D. P., da Cruz, I. H., da Silva Batista, M., & Fabiano, D. P. (2021). Fe_2O_3/MCM-41 as catalysts for methyl orange degradation by Fenton-like reactions. *Environmental Progress & Sustainable Energy, 40*, 13507.
Subramani, R., Izquierdo-Alvarez, A., Bhattacharya, P., Meerts, M., Moldenaers, P., Ramon, H., & Van Oosterwyck, H. (2020). The influence of swelling on elastic properties of polyacrylamide hydrogels. *Frontiers in Materials, 7*, 212.
Tallawi, M., & Germann, N. (2020). Self-crosslinked hydrogel with delivery carrier obtained by incorporation of oxidized alginate microspheres into gelatin matrix. *Materials Letters, 263*, Article 127211.
Topuz, F., Henke, A., Richtering, W., & Groll, J. (2012). Magnesium ions and alginate do form hydrogels: A rheological study. *Soft Matter, 8*, 4877.
Tschoegl, N. W., Knauss, W. G., & Emri, I. (2002). Poisson's ratio in linear viscoelasticity – A critical review. *Mechanics of Time Dependent Materials, 6*(1), 3–51.
Vedovello, P., Sanches, L. V., da Silva Teodoro, G., Ferraz Majaron, V., Bortoletto-Santos, R., Ribeiro, C., & Ferrari Putti, F. (2024). An overview of polymeric hydrogel applications for sustainable agriculture. *Agriculture, 14*, 840.
Wang, P., Luo, Z., & Xiao, Z. (2021). Preparation, physicochemical characterization and in vitro release behavior of resveratrol-loaded oxidized gellan gum/resistant starch hydrogel beads. *Carbohydrate Polymers, 260*, Article 117794.
Wang, S., Liu, J., Wang, L., Cai, H., Wang, Q., Wang, W., Shao, J., & Dong, X. (2023). Underwater adhesion and anti-swelling hydrogels. *Advanced Materials Technology, 8*, Article 2201477.
Wingstrand, S. L., Alvarez, N. J., Hassager, O., & Dealy, J. M. (2016). Oscillatory squeeze flow for the study of linear viscoelastic behaviour. *Journal of Rheology, 60*, 407–418.
Wu, Z., Ding, Q., Wang, H., Ye, J., Luo, Y., Yu, J., … Wu, J. (2024). A humidity-resistant, sensitive, and stretchable hydrogel-based oxygen sensor for wireless health and environmental monitoring. *Advanced Functional Materials, 34*, Article 2308280.
Zhang, Y., Zhang, Y., Tang, L., Liu, Z., Jiang, Z., Liu, Y., Zhou, L., & Zhou, X. (2022). Uniaxial compression constitutive equations for saturated hydrogel combined water-expelled behavior with environmental factors and the size effect. *Mechanics of Advanced Materials and Structures, 29*, 7491–7502.
Zvicer, J., Miskovic-Stankovic, V., & Obradovic, B. (2019). Functional bioreactor characterization to assess potentials of nanocomposites based on different alginate types and silver nanoparticles for use as cartilage tissue implants. *Journal of Biomedical Materials Research Part A, 107A*, 755–768.